

Article

Effect of Microstructure on Layered Double Hydroxides Film Growth on Mg-2Zn-xMn Alloy

Yonghua Chen ¹, Wenhui Yao ^{1,2,*} , Liang Wu ^{1,2,*} , Jing Chen ¹ and Fusheng Pan ^{1,2}

¹ College of Materials Science and Engineering, Chongqing University, Chongqing 400044, China; 20190902001t@cqu.edu.cn (Y.C.); cj126789@cqu.edu.cn (J.C.); fspan@cqu.edu.cn (F.P.)

² National Engineering Research Center for Magnesium Alloys, Chongqing University, Chongqing 400044, China

* Correspondence: yaowh2012@cqu.edu.cn (W.Y.); wuliang@cqu.edu.cn (L.W.)

Abstract: The poor corrosion resistance of magnesium (Mg) alloys significantly restricts their wide applications. The preparation of a layered double hydroxides (LDHs) film can provide effective corrosion protection for Mg alloys. Nevertheless, research on the effect of the Mg alloy microstructure on LDHs film growth is paid less attention, which was studied in detail in this work. Herein, a Mg-2Zn-xMn alloy with different Mn contents was produced, and an LDHs film was then synthesized on their surfaces. The addition of Mn causes a different microstructure in the Mg-2Zn-xMn alloy, which is gradually refined with increasing Mn content, further affecting the surface morphology, surface chemistry, and corrosion protection of the LDHs film. When the Mn content is 1 wt.% ($x = 1$), the LDHs film presents the best corrosion protection, with the lowest corrosion current density. No obvious corrosion product could be observed by the naked eyes on the surface. By contrast, severe corrosion occurs on the Mg-2Zn-0Mn alloy ($x = 0$). Finally, the LDHs film growth mechanism was proposed.

Keywords: magnesium alloy; microstructure; LDHs film; corrosion protection; growth mechanism



Citation: Chen, Y.; Yao, W.; Wu, L.; Chen, J.; Pan, F. Effect of Microstructure on Layered Double Hydroxides Film Growth on Mg-2Zn-xMn Alloy. *Coatings* **2021**, *11*, 59. <https://doi.org/10.3390/coatings11010059>

Received: 8 December 2020

Accepted: 29 December 2020

Published: 7 January 2021

Publisher's Note: MDPI stays neutral with regard to jurisdictional claims in published maps and institutional affiliations.



Copyright: © 2021 by the authors. Licensee MDPI, Basel, Switzerland. This article is an open access article distributed under the terms and conditions of the Creative Commons Attribution (CC BY) license (<https://creativecommons.org/licenses/by/4.0/>).

1. Introduction

As an important structural material, magnesium (Mg) possesses many excellent properties, such as low density, good electromagnetic shielding, and abundant reserves, but its plasticity at room temperature is poor [1,2]. Alloying can effectively improve its plasticity. Recently, the Mg-Zn-Mn alloy presents great application potential in many fields such as the aerospace, automotive, architecture, and biomedical industries because of its high strength, high plasticity, and age hardening [3,4].

Although the second phase can increase the plasticity and strength of alloys, its appearance reduces the corrosion resistance of alloys owing to the low electrode potential of the Mg matrix [5]. Forming a protective coating is one of strategies to improve the corrosion resistance of Mg alloys [6,7]. In recent years, a layered double hydroxides (LDHs) film, whose general formula is $[M^{2+}_{1-x}M^{3+}_x(OH)_2]^{x+}(A^{n-})_{x/n} \cdot mH_2O$, where M^{2+} and M^{3+} , respectively, represent divalent and trivalent metal cations, has attracted much attention in the corrosion protection for Mg alloys [8–13]. A MgAl-LDHs film was in situ produced on AZ31 Mg alloy by Song's group [14]. Zeng et al. [9,10] found that it was only necessary to incorporate a trivalent metal cation to synthesize LDHs on Mg alloys. In Lin et al.'s work [15–17], they analyzed the effect of the divalent/trivalent (M^{2+}/M^{3+}) cation ratio on the growth of the precursor layer on AZ91 Mg alloy.

Most of the research mainly focuses on the effects of solution pH, temperature, and concentration on the corrosion protection of LDHs films [18,19]. However, they ignore the vital influence from the microstructure of Mg alloys, although Tedim et al. confirmed that the uneven distribution of the microstructure could cause the differential growth of ZnAl-LDHs on the AA2024 alloy, consequently affecting its corrosion protection [20,21].

Therefore, this further underlines the necessity to study the effect of the Mg alloy microstructure on the LDHs film growth and its corrosion protection.

Herein, three kinds of extruded Mg-2Zn- x Mn ($x = 0, 1, 2$) alloys with different Mn contents were produced to generate different microstructures in the Mg alloy. Thereafter, LDHs films were in situ synthesized on their surfaces to investigate the effect of the alloy microstructure on the surface morphology, chemical composition, and corrosion protection of the LDHs film on the Mg alloy. Finally, the LDHs film growth mechanism on the Mg alloys was proposed.

2. Materials and Methods

2.1. Preparation of LDHs Film on Mg Alloy

The preparation of LDHs film on the Mg alloy is presented in Figure 1a, and the detail is explained as follows. The Mg-2Zn- x Mn ($x = 0, 1, 2$) alloys were produced by melting metallic (Mg ≥ 99.95 wt.%, Zn ≥ 99.95 wt.%, and Mn ≥ 99.95 wt.%) powders in the electric furnace under the mixed gas of CO₂ and SF₆, named, respectively, ZM20, ZM21, and ZM22. Table 1 lists their chemical compositions. Some impurity elements (such as Fe < 0.03 wt.%, Ni < 0.07 wt.%, Cu < 0.04 wt.%, Si < 0.1 wt.%, Ca < 0.05 wt.%) were present in the alloys. The lower impurity content has little effect on the research of corrosion performance, and these impurity elements can be ignored. Prior to the extrusion, they were pre-heated at 280 °C for 1.5 h. Figure 1b displays the schematic diagram of the extrusion process. The extrusion rate and ratio were 2.5 m·min⁻¹ and 25:1, respectively. After the extrusion deformation, they were cut into samples with a size of 20 × 20 × 2 mm. They were then polished, degreased, and alkaline washed for further treatment.

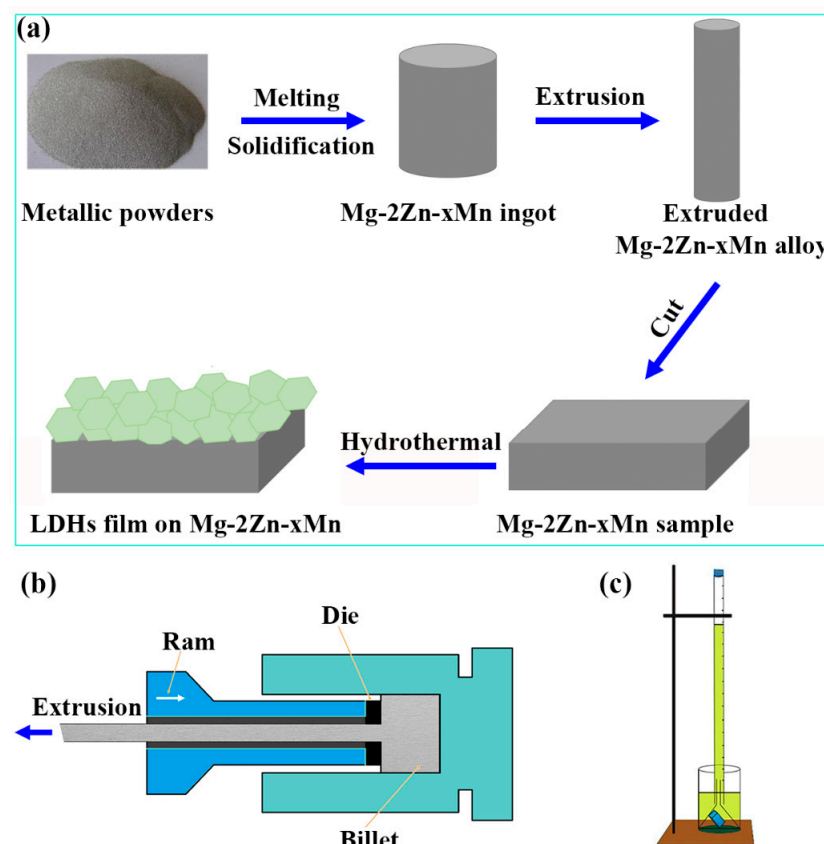


Figure 1. (a) Schematic diagram of preparation process of LDHs film on magnesium alloy. (b) Schematic diagram of the extrusion process. (c) Schematic diagram of the device to evaluate hydrogen evolution.

Table 1. The weight percentage (upper row) of metallic powders for preparation of Mg-2Zn-xMn alloy and their real corresponding percentage (lower row).

Samples	Name	Zn (wt.%)	Mn (wt.%)	Mg (wt.%)
Mg-2Zn	ZM20	1.95	0	Bal.
		1.6	0	98.4
Mg-2Zn-Mn	ZM21	1.97	0.84	Bal.
		1.8	0.9	97.3
Mg-2Zn-2Mn	ZM22	1.94	1.87	Bal.
		1.6	1.9	96.5

In order to synthesize LDHs on Mg alloys, a mixture of 0.3 M NH_4NO_3 and 0.05 M $\text{Al}(\text{NO}_3)_3$ was dissolved in deionized water with vigorous stirring for 15 min, and the solution pH was adjusted to 10.7. The Mg alloy was immersed into the solution and then transferred to a Teflon-lined autoclave, which was then sealed and placed in an oven at 125 °C for 12 h. After that, the samples were cleaned with deionized water and dried at 60 °C for 2 h.

2.2. Characterization

The Mg alloy samples were successively abraded from 200 to 2000 grit using silicon carbide sandpaper, and then they were polished by a polishing machine (MP-2, Ningbo, China) to a mirror finish. Subsequently, they were etched by a reagent consisting of 2.5 g picric acid + 3 mL acetic acid + 21 mL ethanol so that they could be observed with a metallographic microscope (DM2700M, Leica, Germany). The surface morphology was examined by a scanning electron microscope (SEM, JSM-6700F, JEOL, Tokyo, Japan), with an accelerating voltage of 5 kV. The X-ray diffraction (XRD) pattern was collected by an X-ray diffractometer (Rigaku D/max, Rigaku, Tokyo, Japan) equipped with Cu $K\alpha$ radiation ($\lambda = 1.5418 \text{ \AA}$). The chemical composition was analyzed by an energy dispersive spectrometer (EDS, INCA Energy 350, Oxford, Abingdon, UK) and Fourier transform infrared absorption spectrometer (FTIR, NiCOLET-5DX, Thermo Scientific, Waltham, MA, USA). Electrochemical tests were performed by an electrochemical workstation (PARSTAT 4000A, Berwyn, PA, USA). A typical three-electrode cell system was applied to measure the electrochemical impedance spectra (EIS) and Tafel curve, which was carried out after the open-circuit potential was stable. The amplitude was 10 mV, and the test frequency ranged from 10^5 to 10^{-2} Hz. Subsequently, a potentiodynamic polarization curve was measured at a scan rate of $0.5 \text{ mV}\cdot\text{s}^{-1}$. The tested results were fitted by the software ZSimpWin 3.60. The hydrogen evolution was carried out by a home-made device, as shown in Figure 1c.

3. Results

3.1. Alloy Microstructure

The metallographic microstructures of the as-extruded Mg-2Zn-xMn alloys are presented in Figure 2. Only in the ZM20 alloy (Figure 2a) did complete dynamic recrystallization occur. By contrast, a large number of incomplete dynamic recrystallized grains (i.e., coarse grains) are observed in both ZM21 (Figure 2b) and ZM22 (Figure 2c) alloys. On the other hand, as shown in Figure 2, with increasing Mn content, the alloy microstructure is gradually refined, which was also confirmed in [10], where the alloy microstructure can be refined as there is an increase in the Mn content.

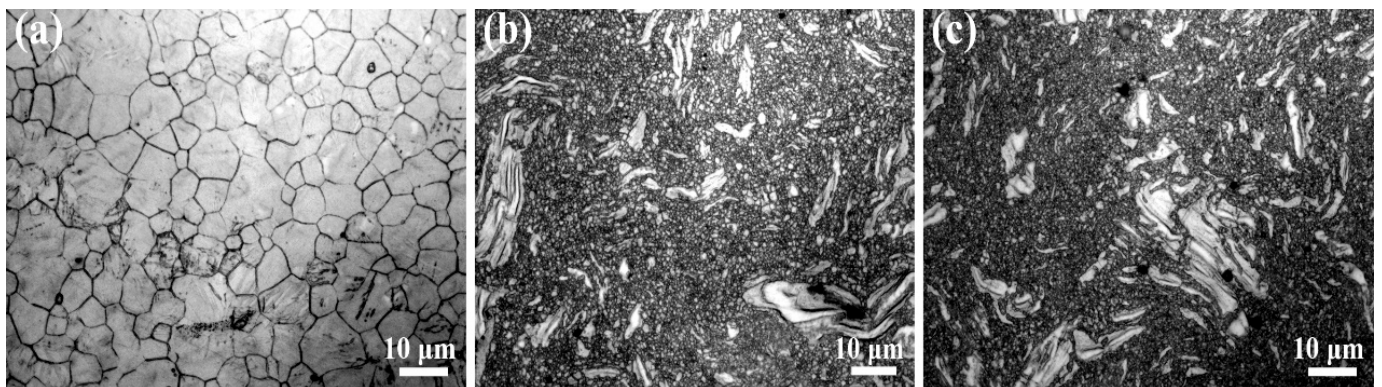


Figure 2. Metallographic images of (a) ZM20, (b) ZM21, and (c) ZM22 alloys.

Further, their SEM images and corresponding EDS results are correspondingly exhibited in Figure S1 (in Supplementary Materials) and Table 1. According to the phase diagram of Mg–Zn–Mn alloy, it is mainly composed of three phases: Mn, α -Mg, and Mg–Zn [4]. Therefore, the second phase in the ZM20 alloy is merely the Mg–Zn phase. Besides the increased Mn content, the content of the Mg–Zn phase is also increased with increasing Mn content, as presented in Table 1. The solid solubility of Mn and Zn in the Mg matrix is less than 0.1% and more than 5% at 300 °C, respectively [21,22]. Thus, the precipitation of Mn may precede the Mg–Zn second phase during the extrusion process, so that it can provide heterogeneous nucleation sites for the Mg–Zn second phase. Consequently, with increasing Mn content, the precipitation of the Mg–Zn phase also increases gradually.

3.2. Surface Morphology of the LDHs Film on Mg Alloy

Compared with the film on the ZM20 alloy (Figure 3a), the films on ZM21 (Figure 3d) and ZM22 (Figure 3g) alloys are more complete, without obvious cracks or holes (Figure 3e,f,h,i). Nevertheless, most of the area of the film on ZM20 alloy is uniformly distributed by numerous nanosheets (Figure 3c). The EDS results (Table 2) show that the main composition of the film is O, Mg, and Al. According to the Mg/Al ratio, it can be concluded that the LDHs film has been successfully formed on the Mg alloy. As for the wide crack on the ZM20 alloy (Figure 3b), it may be ascribed to the stress generated during the LDHs film growth [9]. A few small protrusions are observed on the ZM21-LDHs surface (Figure 3d), while a large number of protrusions with larger size are on the ZM22-LDHs surface shown in Figure 3g. According to their high-magnification images (Figure 3e,f,h,i), the nanosheets still grow perpendicular to the ZM21 alloy, while they seem to collapse on the ZM22 alloy.

Table 2. The atomic percentage of the layered double hydroxides (LDHs) film on Mg alloys.

Samples	O (at.%)	Mg (at.%)	Al (at.%)
ZM20-LDHs	63.9	22.4	13.7
ZM21-LDHs	64.1	23.6	12.3
ZM22-LDHs	62.6	23.2	14.3

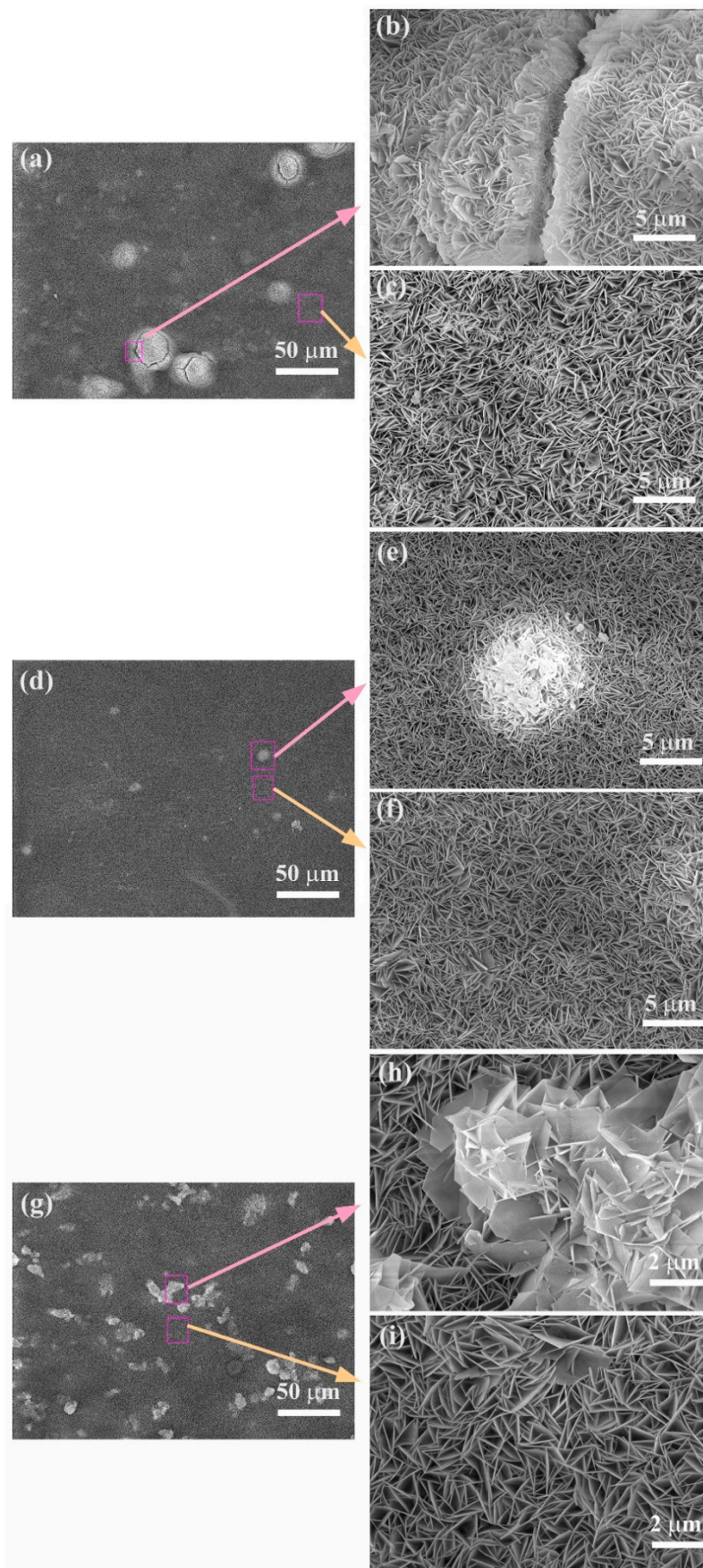


Figure 3. SEM images of the surface morphology of (a–c) ZM20-LDHs, (d–f) ZM21-LDHs, and (g–i) ZM22-LDHs films.

The presentative cross-sectional morphology of the LDHs film is presented in Figure 4. In order to ensure the accuracy, three~five samples were prepared to measure their thickness. The film thickness on the ZM20 alloy is the largest, about 2.7 μm . With increasing Mn content, the film thickness is correspondingly decreased to 1.6 μm on the ZM21 alloy (Figure 4b) and 1.4 μm on the ZM22 alloy (Figure 4c). This is probably because the increasing Mn causes the difference in the electrode potential between the α -Mg and the Mg-Zn phases to decrease, and the number of the formed micro-battery also decreases. Consequently, not enough Mg^{2+} could be provided for the growth of the LDHs film, so the film thickness gradually decreases with increasing Mn content.

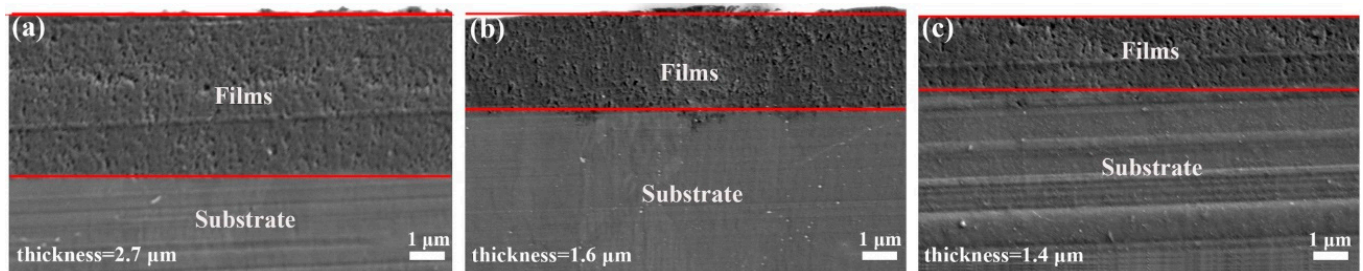


Figure 4. Cross-sectional morphology of the (a) ZM20-LDHs, (b) ZM21-LDHs, and (c) ZM22-LDHs films.

3.3. Surface Chemistry of the LDHs Film on Mg Alloy

Figure 5a reveals the XRD patterns of the LDHs film on Mg alloys. The characteristic diffraction peaks of the (003) and (006) planes at 11.7° and 23.3° further indicate MgAl-LDHs films are successfully prepared on these three alloys. As the Mn content increases, the position of the characteristic peak remains unchanged, so the spacing between crystal planes is almost the same. In addition to the characteristic peaks of the LDHs film, the strong $\text{Mg}(\text{OH})_2$ peaks are also detected in Figure 5a, demonstrating the developed film also contains $\text{Mg}(\text{OH})_2$.

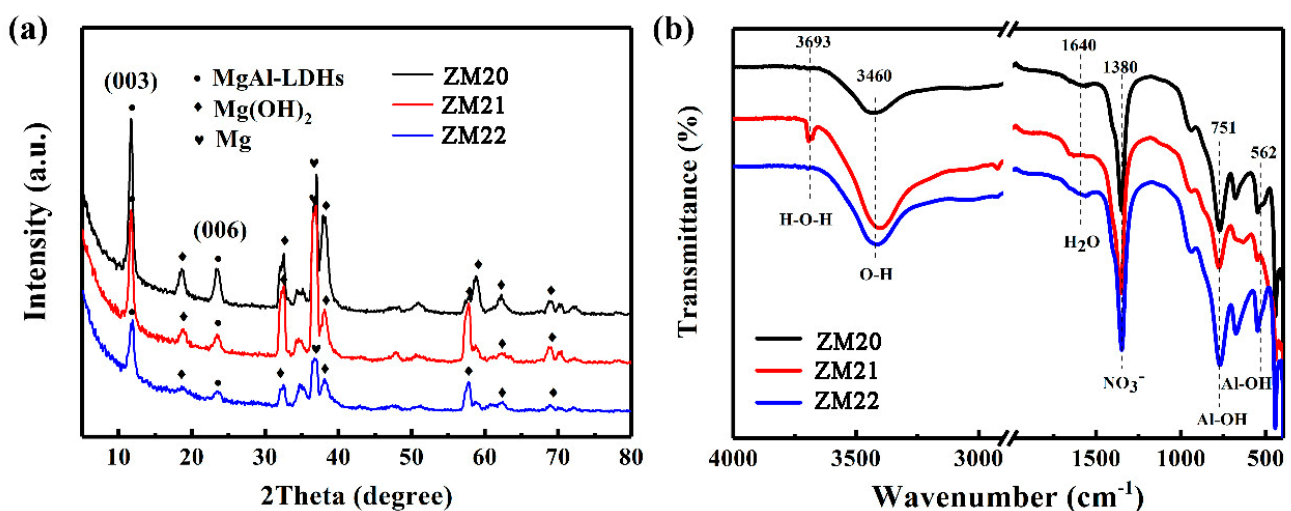


Figure 5. (a) XRD patterns and (b) FTIR spectra of ZM20-LDHs, ZM21-LDHs, and ZM22-LDHs films.

The FTIR spectra were used to further evaluate the surface chemistry, as presented in Figure 5b. The wide absorption band at 3460 cm^{-1} is assigned to the asymmetric and symmetric stretching vibrations of water molecules. The sharp band at 3693 cm^{-1} is related to the stretching vibrations of $-\text{OH}$ groups. The strong absorption peaks near 1380 cm^{-1} are the asymmetric tensile peaks of NO_3^- in the intercalation [23]. The higher the Mn content, the sharper the tensile peak of NO_3^- . Other adsorption bands below

800 cm^{-1} are associated with the metal-oxygen (M–O) stretching and bending modes in the brucite-like lattice.

3.4. Corrosion Protection of the LDHs Film on Mg Alloy

The Tafel polarization curve is exhibited in Figure 6, and the electrochemical parameters are correspondingly listed in Table 3. According to the corrosion current density, the corrosion rate can be arranged in the following sequence: ZM20-LDHs ($1.8\ \mu\text{A}\cdot\text{cm}^{-2}$) > ZM22-LDHs ($1.1\ \mu\text{A}\cdot\text{cm}^{-2}$) > ZM21-LDHs ($0.4\ \mu\text{A}\cdot\text{cm}^{-2}$). In addition, the LDHs film on the ZM21 alloy possesses the highest corrosion potential, with a value of -0.22 vs. SCE, further indicating it can provide the best corrosion protection for the Mg alloy. This is related to its dense surface morphology as shown in Figure 3d–f. Considering the surface morphology of the ZM22-LDHs film, it can offer moderate corrosion protection for the ZM22 alloy. By contrast, the corrosion protection of the LDHs film for the ZM20 alloy is the worst in this work. Although the thickness of the LDHs film on ZM20 is the thickest ($2.7\ \mu\text{m}$), there exist many cracks on its surface, providing paths for the corrosive ions to penetrate into the film to reach the Mg alloy. Therefore, the corrosion protection of the ZM20-LDHs film for the Mg alloy is deteriorated, with the largest corrosion current density and the lowest corrosion potential.

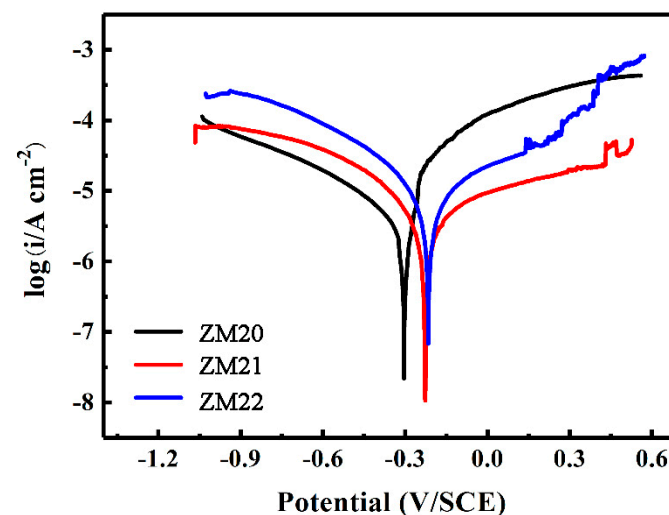


Figure 6. Tafel polarization curves of ZM20-LDHs, ZM21-LDHs, and ZM22-LDHs films in 3.5 wt.% NaCl solution.

Table 3. Corrosion potential (E_{corr}) and corrosion current density (i_{corr}) of the samples according to the Tafel polarization curve.

Samples	E_{corr} (V _{SCE})	i_{corr} ($\mu\text{A}\cdot\text{cm}^{-2}$)
ZM20-LDHs	-0.35	1.8
ZM21-LDHs	-0.22	0.4
ZM22-LDHs	-0.23	1.1

In order to better analyze their corrosion behavior, EIS spectra were measured, as shown in Figure 7. From Figure 7a, the resistance sequence is as follows: ZM21-LDHs > ZM22-LDHs > ZM20-LDHs. The LDHs film on the ZM21 alloy provides the best corrosion protection for the Mg alloy, while the film on ZM20 provides the worst corrosion protection, which is consistent with the Tafel results. In particular, the equivalent circuit is the inset in Figure 7a. The Bode phase angle diagram (Figure 7b) discloses that all samples have two time constants, correspondingly representing the LDHs film capacitance C_{out} and the interface oxide layer capacitance C_{inn} . The electrochemical behavior of the thin film is not exactly capacitive, so C is replaced by CPE and n refers to the similarity. It is found from

the detailed fitting data (Table 4) that the R_{inn} values for all samples are larger than R_{out} . The interface oxide layer can be used to represent the overall corrosion resistance because it is the closest to the substrate. Among these three samples, the R_{inn} value of ZM21-LDHs is the largest, up to $8.01 \times 10^3 \Omega$, further confirming its best corrosion protection for the ZM21 alloy.

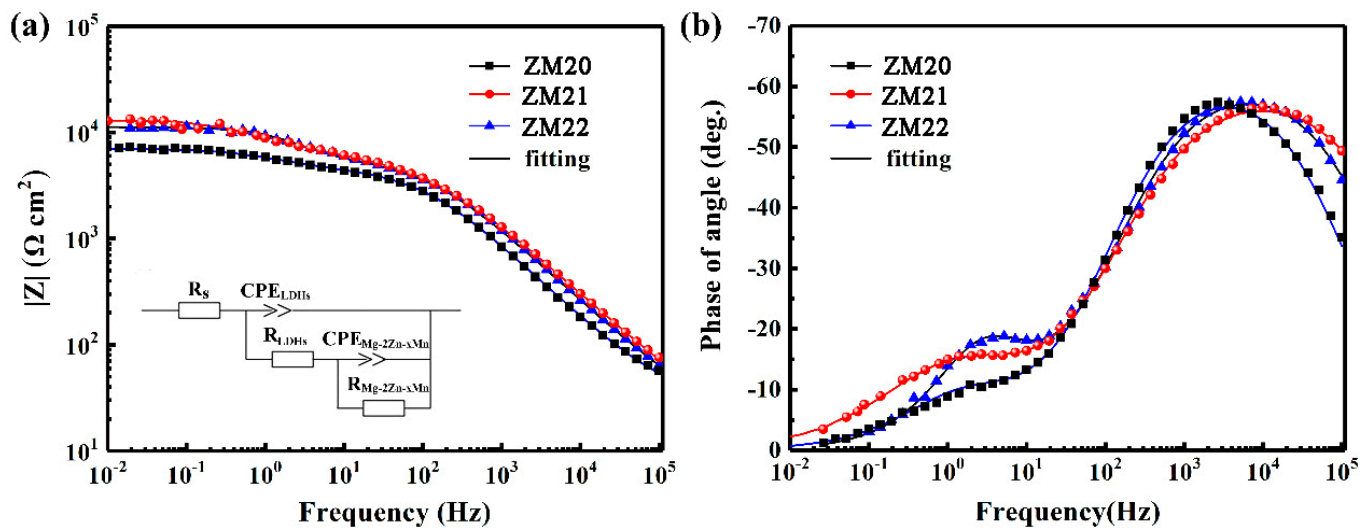


Figure 7. Bode plots of (a) $|Z|$ and (b) phase angle vs. frequency for various specimens after 30 min immersion in 3.5 wt.% NaCl solution. Inset in Figure 7a is the equivalent circuit.

Table 4. Corrosion potential (E_{corr}) and corrosion current density (i_{corr}) of the samples according to the Tafel polarization curve.

Samples	R_{sol} ($\Omega \cdot \text{cm}^2$)	CPE_{out} ($\mu\text{F} \cdot \text{cm}^{-2}$)	n_{out}	R_{out} ($\Omega \cdot \text{cm}^2$)	CPE_{inn} ($\mu\text{F} \cdot \text{cm}^{-2}$)	n_{inn}	R_{inn} ($\Omega \cdot \text{cm}^2$)	X^2 $\times 10^{-3}$
ZM20-LDHs	30.44	2.05×10^{-6}	0.72	2.46×10^3	10.4×10^{-5}	0.71	4.58×10^3	3.1
ZM21-LDHs	15.75	1.87×10^{-6}	0.68	5.94×10^3	5.57×10^{-5}	0.61	8.01×10^3	8.3
ZM22-LDHs	21.62	1.66×10^{-6}	0.70	5.51×10^3	2.25×10^{-5}	0.83	5.72×10^3	9.1

In order to further evaluate the corrosion protection of the developed LDHs film for the Mg-2Zn- x Mn alloy, the samples were immersed in 3.5 wt.% NaCl solution for 7 days. Their SEM images and optical images after the immersion test are, respectively, presented in Figures S2 and S3 (in Supplementary Materials). Serious corrosion occurs on the ZM20-LDHs film. Sesame-sized pitting holes that penetrated through the sample are observed on the ZM20 alloy, and a large amount of white corrosion products are accumulated around the corrosion pit on its surface. As for the ZM21-LDHs film, it is still flat on the ZM21 alloy, free of holes, and no obvious corrosion products can be observed, indicating the LDHs film can effectively protect the Mg alloy substrate from corrosion, consistent with the Tafel and EIS results.

Figure 8 shows the average hydrogen evolution volume of samples in 3.5 wt.% NaCl solution at 25 °C. The total hydrogen release gradually increases with the time for each sample in Figure 8a. The produced hydrogen volume by ZM21-LDHs is the lowest, while that by ZM20-LDHs is the largest, which is still consistent with the above results. From Figure 8b, the hydrogen evolution rate of ZM21-LDHs remains almost unchanged, with the smallest value, further indicating the good protection of LDHs film for the Mg substrate, while the hydrogen evolution rate of ZM20-LDHs is, not surprisingly, gradually increased.

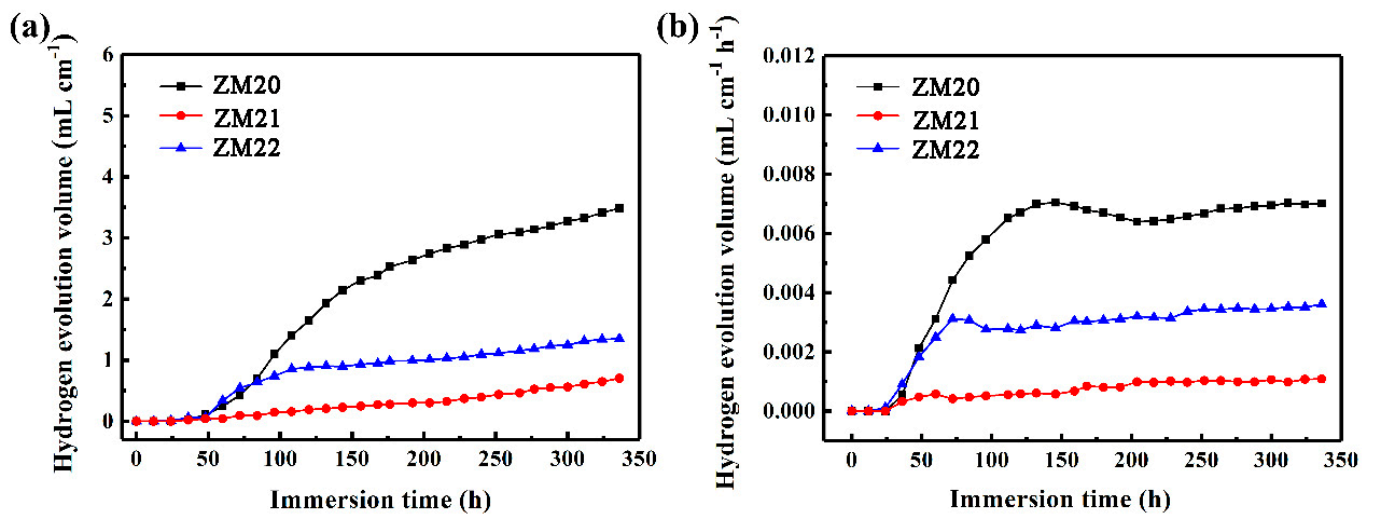


Figure 8. Hydrogen evolution (a) volume and (b) rate of different samples in 3.5 wt.% NaCl solution.

3.5. Formation Mechanism of the LDHs Film on Mg Alloy

The effect of the surface microstructure on the growth behavior of MgAl-LDHs on the Mg alloy is unveiled in Figure 9. Compared with the ZM20 alloy, the addition of Mn provides nucleation sites for the precipitation of the second phase of Mg–Zn, resulting in a smaller grain size and finer dispersion of the second phase. Generally, the finer the grain, the better the corrosion resistance of the material, and the less Mg²⁺ can be dissolved. The in situ growth of the LDHs film strongly depends on the dissolution of the Mg matrix. Therefore, the LDHs film is much thinner with the increasing Mn content, as shown in Figure 4.

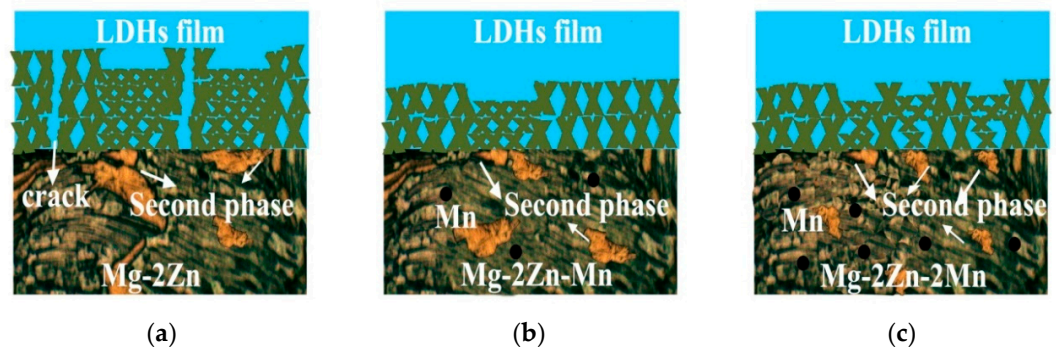


Figure 9. Schematic illustrating the growth mechanism of the Mg–Al LDHs films on Mg alloys with different alloy microstructures.

As for the sample itself, the second phase acts as a cathode in the Mg–Zn–*x*Mn alloy, increasing the potential difference with the Mg matrix and resulting in micro-galvanic corrosion. Thus, the local dissolved Mg²⁺ is increased, which is beneficial to the growth of the LDHs film. Consequently, the growth rate of the LDHs film at different regions (with and without the Mg–Zn phase) is different on the ZM20 Mg alloy, resulting in the cracks near the second phase (Figures 3a and 9a). When the Mn content is 1 wt.%, because of the existence of much more second phase with smaller size, the corrosion resistance of the matrix in the local area decreases, the Mg²⁺ source increases, and a few protrusions appear (Figures 3d and 9b). Nevertheless, there is no obvious crack on the film surface, providing good protection for the ZM21 Mg alloy. When the Mn content is increased to 2 wt.%, the second phase of Mg–Zn in the matrix becomes finer and more dispersed. The increase in the number of the second phase leads to the increase in the number

of protrusions (Figures 3g and 9c). The uneven distribution of protrusions decreases the corrosion resistance of the LDHs film on the ZM22 Mg alloy.

4. Conclusions

In this work, an LDHs film was prepared on an as-extruded Mg-2Zn-xMn ($x = 0, 1, 2$) Mg alloy substrate to investigate the influence of the alloy microstructure on the film growth mechanism and performance. During the extrusion process, the ZM20 alloy underwent complete dynamic recrystallization; the addition of Mn provided a large number of nucleation sites for recrystallization, and the grains were refined, causing the formed LDHs film to be thinner and denser. This is beneficial to the corrosion protection for the Mg alloy. Among these three samples, the LDHs film on ZM21 presents the best corrosion protection, with the lowest corrosion current of $0.4 \mu\text{A}\cdot\text{cm}^{-2}$ and the largest corrosion potential of -0.22 vs. SCE. Consequently, no obvious corrosion product could be observed on the ZM21 after immersion in 3.5 wt.% NaCl solution for 7 days. By contrast, sesame-sized pits appeared on ZM20, through the whole sample, which were related to the cracks on the LDHs film surface. The LDHs film on the ZM22 alloy provides moderate corrosion protection, associated with a large amount of protrusions on its surface. Therefore, a suitable Mn content can effectively improve the corrosion resistance of the Mg alloy, while the corrosion resistance can be decreased if the Mn content is too high. This work confirms the necessity to study the effect of the alloy microstructure on the LDHs film growth, which would improve the corrosion resistance of Mg alloys to accelerate their wide applications in practice.

Supplementary Materials: The following are available online at <https://www.mdpi.com/2079-6412/11/1/59/s1>, Figure S1: SEM images and EDS results of Mg alloys of ZM20, ZM21, and ZM22. Figure S2: SEM images and EDS results of LDHs films on Mg alloy after the immersion test for 7 days. Figure S3: Optical images of samples after the immersion test.

Author Contributions: Conceptualization, L.W.; methodology, J.C.; writing—original draft preparation, Y.C.; writing—review and editing, W.Y.; supervision, F.P.; project administration, L.W. and W.Y.; funding acquisition, W.Y. and L.W. All authors have read and agreed to the published version of the manuscript.

Funding: This work was supported by the National Natural Science Foundation of China (51971040, 51701029), the Fundamental Research Funds for the Central Universities (2020CDJQY-A007), China Postdoctoral Science Foundation Funded Project (2017M620410, 2018T110942), the Chongqing Postdoctoral Scientific Research Foundation (Xm2017010).

Data Availability Statement: Available upon request from the corresponding author.

Conflicts of Interest: The authors declare no conflict of interest.

References

1. Wu, Z.; Ahmad, R.; Yin, B.; Sandlöbes, S.; Curtin, W. Mechanistic origin and prediction of enhanced ductility in magnesium alloys. *Science* **2018**, *359*, 447–451. [[CrossRef](#)]
2. Liu, H.; Li, Y.; Zhang, K.; Li, X.; Ma, M.; Shi, G.; Yuan, J.; Wang, K. Microstructure, hot deformation behavior, and textured evolution of Mg-3 wt%Zn-1 wt%Ca-0.5 wt% Sr alloy. *J. Mater. Sci.* **2020**, *55*, 12434–12447. [[CrossRef](#)]
3. Wu, J.; Chen, J.; Yan, H.; Xia, W.; Su, B.; Yu, L.; Liu, G.; Song, M. Enhancing the mechanical properties of high strain rate rolled Mg-6Zn-1Mn alloy by pre-rolling. *J. Mater. Sci.* **2017**, *52*, 10557–10566. [[CrossRef](#)]
4. Hu, K.; Liao, Q.; Li, C.; Le, Q.; Zhou, W.; Cheng, C.; Ning, S.; Chen, X.; Yu, F. High ductility induced by un-DRXed grains in a Mg-Zn-Mn-La-Ce alloy. *J. Mater. Sci.* **2020**, *54*, 10902–10917. [[CrossRef](#)]
5. Zhou, Z.; Li, C.; Shen, L.; Bao, N. Ion-exchange modification of potassium magnesium titanate for high-performance wear-corrosion-resistant composite coatings. *J. Mater. Sci.* **2020**, *55*, 13836–13851. [[CrossRef](#)]
6. Nezamdoust, S.; Seifzadeh, D.; Rajabalizadeh, Z. Application of novel sol-gel composites on magnesium alloy. *J. Magnes. Alloy.* **2019**, *7*, 419–432. [[CrossRef](#)]
7. Yao, W.; Wu, L.; Huang, G.; Jiang, B.; Atrens, A.; Pan, F. Superhydrophobic coatings for corrosion protection of magnesium alloys. *J. Mater. Sci. Technol.* **2020**, *52*, 100–118. [[CrossRef](#)]
8. Shulha, T.; Serdechnova, M.; Lamaka, S.; Wieland, D.; Lapko, K.; Zheludkevich, M. Chelating agent-assisted in situ LDH growth on the surface of magnesium alloy. *Sci. Rep.* **2018**, *8*, 16409. [[CrossRef](#)]

9. Zeng, R.; Liu, Z.; Zhang, F.; Li, S.; He, Q.; Cui, H.; Han, E. Corrosion resistance of in-situ Mg–Al hydrotalcite conversion film on AZ31 magnesium alloy by one-step formation. *Trans. Nonferrous Met. Soc. China* **2015**, *25*, 1917–1925. [[CrossRef](#)]
10. Seifzadeh, D.; Farhoudi, L. Electroless Co–P plating on magnesium alloy and its anti-corrosion properties. *Surf. Eng.* **2016**, *32*, 348–355. [[CrossRef](#)]
11. Niu, Y.; Hou, J.; Ning, F.; Chen, X.; Jia, Y.; Le, Q. Hot deformation behavior and processing map of Mg-2Zn-1Al-0.2RE alloy. *J. Rare Earth* **2020**, *38*, 665–675. [[CrossRef](#)]
12. Zhang, Y.; Li, J.; Liu, Y.; Chen, L. Microstructure characteristics, film layer rupture mechanism and corrosion behavior of hot-rolled Mg-2Zn-0.2Mn-xNd. *Mater. Charact.* **2020**, *165*, 110368. [[CrossRef](#)]
13. Chen, X.; Wang, H.; Le, Q.; Jia, Y.; Zhou, X.; Yu, F.; Atrens, A. The role of long-period stacking ordered phase on the discharge and electrochemical behaviors of magnesium anode Mg–Zn–Y for the primary Mg–air battery. *Int. J. Energy Res.* **2020**, *44*, 8865–8876. [[CrossRef](#)]
14. Petrova, E.; Serdechnova, M.; Shulha, T.; Lamaka, S.; Wieland, D.; Karlova, P.; Blawert, C.; Starykevich, M.; Zheludkevich, M. Use of synergistic mixture of chelating agents for in situ LDH growth on the surface of PEO-treated AZ91. *Sci. Rep.* **2020**, *10*, 8645. [[CrossRef](#)]
15. Cheng, S.; Zhang, D.; Li, M.; Liu, X.; Zhang, Y.; Qian, S.; Peng, F. Osteogenesis, angiogenesis and immune response of Mg–Al layered double hydroxide coating on pure Mg. *Bioact. Mater.* **2021**, *6*, 91–105. [[CrossRef](#)] [[PubMed](#)]
16. Yin, X.; Mu, P.; Wang, Q.; Li, J. Superhydrophobic ZIF-8-based dual-layer coating for enhanced corrosion protection of Mg alloy. *ACS Appl. Mater. Interfaces* **2020**, *12*, 35453–35463. [[CrossRef](#)]
17. Lin, J.; Jeng, K.; Uan, J. Crystallization of a chemical conversion layer that forms on AZ91D magnesium alloy in carbonic acid. *Corros. Sci.* **2011**, *53*, 3832–3839. [[CrossRef](#)]
18. Iqbal, M.; Fedel, M. Effect of synthesis conditions on the controlled growth of MgAl-LDH corrosion resistance film: Structure and corrosion resistance properties. *Coatings* **2019**, *9*, 30. [[CrossRef](#)]
19. Wu, L.; Pan, F.; Liu, Y.; Zhang, G.; Tang, A.; Atrens, A. Influence of pH on the growth behaviour of Mg–Al LDH films. *Surf. Eng.* **2018**, *34*, 674–681. [[CrossRef](#)]
20. Tedim, J.; Zheludkevich, M.; Salak, A.; Lisenkov, A.; Ferreira, M. Nanostructured LDH-container layer with active protection functionality. *J. Mater. Chem.* **2011**, *21*, 15464. [[CrossRef](#)]
21. Campestrini, P.; Westing, E.; Rooijen, H.; Wit, J. Relation between microstructural aspects of AA2024 and its corrosion behaviour investigated using AFM scanning potential technique. *Corros. Sci.* **2000**, *42*, 1853–1861. [[CrossRef](#)]
22. Komatsu, S.; Ikeda, M.; Mori, U. Solidus composition in Mg side phase diagram of Mg–Zn binary system and its estimation method. *J. Jpn. Inst. Light Met.* **2004**, *54*, 25–30. [[CrossRef](#)]
23. Zhang, G.; Wu, L.; Tang, A.; Ma, Y.; Song, G.; Zheng, D.; Jiang, B.; Atrens, A.; Pan, F. Active corrosion protection by a smart coating based on a MgAl-layered double hydroxide on a cerium-modified plasma electrolytic oxidation coating on Mg alloy AZ31. *Corros. Sci.* **2018**, *32*, 370–382. [[CrossRef](#)]